BMC Chemistry

RESEARCH

Open Access

Magnetic graphene oxide nanosheets with amidoamine dendronized crosslinks for dual pH and redox-sensitive doxorubicin delivery

Amir Reza Sarikhani[2,5†], Mehdi Abedi[1,4†], Samira Sadat Abolmaali[1,2], Sedigheh Borandeh[2] and Ali Mohammad Tamaddon[1,2,3*]

Abstract

Delivering anticancer drugs to the appropriate site within the body poses a critical challenge in cancer treatment with chemotherapeutic agents like doxorubicin (DOX). Magnetic graphene oxide (GO) nanosheets with generation 1 (G1) amidoamine-dendronized crosslinks were developed by coupling cystamine-functionalized GO nanosheets with Fe3O4 nanoparticles modified with primary amine and methyl acrylate. These magnetic GO nanosheets were loaded with DOX to create a dual pH- and redox-responsive delivery system for cancer chemotherapy. The prepared magnetic nanosheets underwent characterization using FTIR, XRD, DLS, VSM, FE-SEM, and TEM. Physical DOX adsorption was evaluated using various isotherms, including Langmuir, Freundlich, Temkin, and Dubinin-Radushkevich. The in-vitro release profiles of DOX from the magnetic nanosheets were studied under different pH conditions, with and without glutathione (GSH), and the drug release data were fitted with various kinetic models. Additionally, an MTT assay was employed to assess the compatibility and antitumor activity of DOX-loaded magnetic nanosheets in the HepG2 cell line. The results showed that the maximum drug loading was 13.1% (w/w) at a drug/carrier ratio of 1. Without GSH addition, the maximum drug release after 10 days was only 17.9% and 24.1% at pH 7.4 and 5.3, respectively. However, in the presence of GSH, the maximum drug release reached 51.7% and 64.8% at pH 7.4 and 5.3, respectively. Finally, the research findings suggest that the magnetic nanosheets exhibited pH- and redox-stimuli drug release, high biocompatibility, and superior antitumor activity compared to free DOX.

Keywords Superparamagnetic nanoparticle, Fe_3O_4, Drug release kinetic, Stimuli-responsive, Redox, Graphene oxide, Doxorubicin

†Amir Reza Sarikhani and Mehdi Abedi are co-first author, these authors have equally contributed to the work.

*Correspondence:
Ali Mohammad Tamaddon
amtamadon@gmail.com; amtamadon@sums.ac.ir
[1]Department of Pharmaceutical Nanotechnology, School of Pharmacy, Shiraz University of Medical Sciences, Shiraz, Iran
[2]Center for Nanotechnology in Drug Delivery, Shiraz School of Pharmacy, Shiraz University of Medical Sciences, Shiraz 71345, Iran
[3]Department of Pharmaceutics, School of Pharmacy, Shiraz University of Medical Sciences, Shiraz 71345, Iran
[4]Present address: Pharmaceutical Sciences Research Center, Shiraz University of Medical Sciences, Shiraz 71345, Iran
[5]Student Research Committee, Shiraz University of Medical Sciences, Shiraz, Iran

Introduction

Globally, cancer is one of the most common causes of mortality, resulting from abnormal cell growth [1]. Unregulated cellular growth and invasion inhibit the death of cells, facilitating their spread to other tissues where they form malignant tumors [2]. Due to the global impact of cancer, it is crucial to investigate various treatment options and new medications [3]. Currently, conventional cancer treatments include surgery, radiation, targeted therapy, and immunotherapy. Although effective in eliminating or controlling tumor growth, recurrence, and metastasis to a variable extent, these treatments can cause serious complications. Some natural or semi-synthetic compounds, such as paclitaxel, camptothecin, and doxorubicin (DOX) have been widely used to treat cancers [4]. However, cancer cells can demonstrate resistance to these agents through various cellular efflux pumps or pump-independent mechanisms. These pumps such as p-glycoprotein transport DOX out of the cell, decreasing the accumulation of the drug inside the cell [5, 6]. Various methods of drug delivery and targeting, including passive and active strategies, take advantage of the unique characteristics of tumors. These characteristics include abnormal blood vessels, overexpression of specific receptors, and altered tumor environments. These features enable the retention and accumulation of drugs within the tumor site [7]. Due to the drawbacks of conventional chemotherapeutics, such as limited therapeutic efficacy and a broad spectrum of side effects, developing novel delivery systems becomes imperative. Nanomaterials have unique properties enabling unique phenomena and various applications. The combination of pharmacology and nanotechnology has led to the development of novel medications for combating different advanced or metastatic cancers [8].

Nanomedicine has seen significant advancements, offering controlled drug release, reduced side effects, targeted delivery, and enhanced drug stability. A diverse array of drug delivery systems has been explored [9, 10], including metals and metal oxides like gold [11], silver [12], and iron oxides [13], as well as silica nanoparticles [14], micelles [15, 16], vesicles [17], dendrimers [18], hydrogels [19], carbon nanotubes [20], quantum dots [21], and graphene oxide [22] that are utilized for the delivery of various anticancer agents like DOX. Among these carriers, magnetic nanoparticles have attracted great interest in drug delivery applications. They can be used as an external stimulus to release drugs in the drug delivery system by taking advantage of the appropriate permeability of electromagnetic waves to living organisms. For improved therapeutic outcomes, a magnet is positioned near the treatment site, such as a tumor, to facilitate the local accumulation of nanocarriers and drugs [19]. Additionally, magnetic nanoparticles (NPs) are anticipated to synergistically enhance therapeutic effects through the magnetic hyperthermia effect [23].

Recently, graphene and graphene oxide (GO) have garnered significant attention from researchers in the field of nanomedicine due to their unique properties, biocompatibility, small size, responsiveness to stimuli, large surface area, and ease of modification [24]. GO nanosheets possess numerous hydroxyl, carboxyl, and epoxy groups, making them more readily functionalized through non-covalent or chemical bonding. The non-covalent interaction of GO primarily relies on electrostatic forces, van der Waals forces, π-π stacking, and hydrophobic interactions [25]. The functional groups allow for GO functionalization through various chemical reactions, including diazotization [26], epoxy ring opening [27], amidation [28], carbodimidization [29], carboxylic acylation [30], etc. Additionally, the functionalization of GO is crucial for overcoming colloidal stability issues [31]. Furthermore, chemical modification of GO offers the potential for drug loading and release in a controlled manner.

Recently, several magnetic metal oxide-graphene composites exhibiting superior delivery performance due to the combined effects of the metal oxides and graphene have been reported for drug delivery [32, 33]. Polymer-modified Fe_3O_4-GO composites have shown pH- and magnetic field-sensitive drug delivery [34]. In another study, a DOX-loaded PEGylated magnetic GO nanocomposite was prepared, which responds to an external magnetic field for magnetic resonance imaging [35]. However, before conducting in-vivo experiments, several factors should be addressed, including achieving uniform and stable composites, optimizing drug loading and release kinetics, and ensuring compatibility and cellular activity. Additionally, tumor tissues are known to possess elevated levels of reducing agents like glutathione (GSH) compared to normal tissues. Capitalizing on this distinction, redox-sensitive delivery systems employ GSH-responsive linkers or moieties that undergo cleavage in high GSH concentrations. This mechanism facilitates targeted drug release within tumor cells, thereby minimizing systemic exposure and mitigating off-target effects. Therefore, our study aimed to develop GSH-responsive magnetic GO nanosheets capable of efficiently loading and releasing DOX in a manner sensitive to both pH and redox conditions.

Materials and methods

Materials

Graphite (particle size = 70 μm, purity = 99.999%), ammonia 25% solution, N, N-dimethylformamide (DMF), hydrogen peroxide (H_2O_2), dimethyl sulfoxide (DMSO), ferric chloride hexahydrate ($FeCl_3{\cdot}6H_2O$), ferrous chloride tetrahydrate ($FeCl_2{\cdot}4H_2O$), potassium permanganate ($KMnO_4$), sodium nitrate ($NaNO_3$), (3-aminopropyl)

triethoxysilane (APTES), and citric acid were supplied by Merck (Germany). GSH, carbonyl diimidazole (CDI), methyl acrylate, triethylamine (TEA), fetal bovine serum (FBS), MTT reagent, RPMI 1640 medium, and penicillin-streptomycin solution were obtained from Sigma Aldrich (USA). Cystamine (Cys) was supplied by Santa Cruz (USA). Doxorubicin (DOXO-cell®) was acquired from Cell Pharm (Georgia). The human HCC cell line HepG2 was purchased from the Pasteur Institute (Tehran, Iran).

Instruments

FT-IR spectra of KBr-compressed pellets were acquired with an FT-IR spectrometer (Vertex, Bruker, Germany) in the range of 400–4000 cm^{-1} at a resolution of 4 cm^{-1}. XRD patterns were obtained using a Bruker D8 advanced diffractometer (Germany). Morphology was examined using transmission electron microscopy (TEM) (Philips, Germany) and field emission scanning electron microscopy (FESEM, TESCAN MIRA3, Brno, Czech Republic). The superparamagnetic properties of the nanoparticles were measured using a vibrating sample magnetometer (VSM) Kavier Kashan (Iran). UV-VIS absorbance was recorded at 480 nm using a Gen 5 UV-Vis microplate reader (BioTek Instruments, Inc., Winooski, VT, USA).

Synthesis of GO and cystamine functionalization

GO was synthesized from graphite powder using the modified Hummer method. Initially, 0.5 g graphite powder was dispersed in 12 ml H_2SO_4 containing 0.25 g $NaNO_3$. Subsequently, 1.5 g $KMnO_4$ was added to the mixture while stirring in an ice bath. The stirring continued at 35 °C until the color of the mixture changed to light brown as the reaction progressed. Then, 25 ml of deionized water was added, and the mixture was stirred at 98 °C. After 1 h, 2 ml H_2O_2 solution was added until the mixture turned yellow. The prepared mixture was filtered and washed with a 10% HCl solution. Finally, the prepared GO was washed 3 times with deionized water and freeze-dried [36]. In the next step, 100 mg prepared GO was dispersed in 3 ml DMSO using bath sonication for 15 min. Subsequently, 0.125 mg of CDI reagent was dissolved in 1 ml of DMSO and added gradually to the GO mixture under a nitrogen atmosphere while stirring for 24 h. Then, 1.25 g of Cys and 1 ml of TEA dissolved in 3 ml of DMSO were added dropwise to the mixture under a nitrogen atmosphere, stirred for another 24 h, centrifuged at 12,000 rpm for 10 min, and washed three times with deionized water as similarly reported elsewhere [37].

Synthesis of Fe3O4 NPs and amine functionalization

Citric acid-capped magnetic iron oxide nanoparticles (Fe_3O_4-CA) were synthesized based on previous studies [38]. Initially, 50 ml of deionized water was degassed for 15 min with N_2 gas. Then, 1.35 g of $FeCl_2{\cdot}4H_2O$ and 3.68 g of $FeCl_3{\cdot}6H_2O$ were dissolved in the degassed water and heated to 80 °C under an N_2 atmosphere. The pH of the reaction was maintained at 10.5 for 2 h by adding 25% ammonia solution. Afterward, 4 ml of citric acid solution (0.5 g/ml) was added to the mixture and stirred for 1 h at 90 °C. The reaction mixture was then cooled, and the prepared nanoparticles were separated using magnetic decantation. The resulting black product was washed three times with deionized water. To synthesize Fe_3O_4-NH_2 NPs, 150 mg of Fe_3O_4-CA was dispersed in 19 ml of deionized water using probe sonication for 20 min and then cooled to room temperature. Subsequently, 60 ml of methanol was added to the mixture, and the temperature increased to 40 °C. The pH was adjusted to 10.5 by adding 25% ammonia solution, and then 1.2 ml of APTES was added dropwise to the mixture and stirred [39]. The nanoparticles were separated using magnet decantation and washed three times with a 25% ethanolic solution [40].

Synthesis of Fe3O4-β-amino acid methyl ester and Fe3O4@GO-Cys

Two milligrams of Fe_3O_4-NH_2 were dispersed in 30 ml of ethanol using probe sonication for 5 min. Then, 1 ml of TEA and 2.5 ml of methyl acrylate were added and stirred at room temperature under reflux conditions. After 5 days, Fe_3O_4-β-amino acid methyl ester NPs were separated by a magnet and washed three times with a 20% ethanolic solution [41]. In the next step, 5 mg of Fe_3O_4-β-amino acid methyl ester and GO-Cys were separately dispersed in 10 ml of deionized water for 20 min by bath sonication and then added to each other under stirring conditions for 6 h. After that, Fe_3O_4@GO-Cys nanoparticles were magnetically separated and washed three times with a 30% ethanolic solution. The separated nanoparticles were dried at 40 °C for 3 days [42].

XRD analysis

The crystalline properties and phase identification of GO, GO-Cys, and Fe_3O_4@GO-Cys were characterized by X-ray diffraction (XRD using a Bruker D8 advanced diffractometer (Germany). The method uses Cu Kα as a source for radiation at 40 kV and 40 mA. The samples were scanned over the angular range of $5° < 2\Theta) < 70°$ values with a scanning speed of 0.5°/min and the sampling interval of 0.02° and acquisition time of 1.0 s/step.

Electron microscopy

The surface morphology was observed through a field emission scanning electron microscope (FESEM, TESCAN MIRA3, Brno, Czech Republic, and (TEM, Philips, Germany) with an acceleration voltage of 80 kV. The FESEM samples were prepared by dropping a dilute

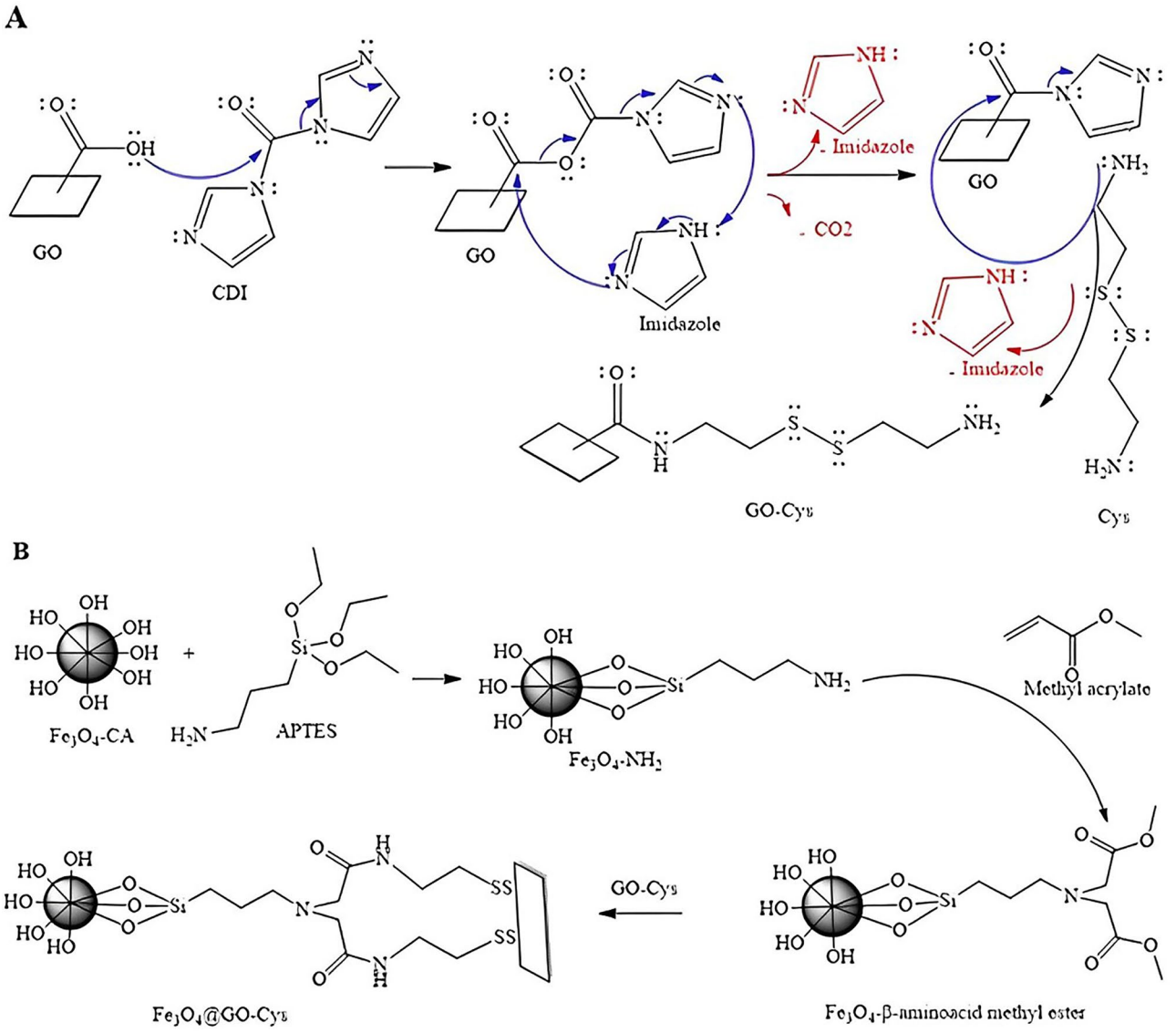

Fig. 1 Schematic presentation of the synthesis of GO-Cys (upper panel), Fe_3O_4-NH_2, Fe_3O_4- β-amino acid methyl ester, and Fe_3O_4@GO-Cys (lower panel)

suspension on a glass and the surface was coated with a thin gold film under vacuum before microscopy scanning. For TEM analysis, the samples were deposited on copper grids of 400 mesh coated with carbon.

DOX loading

DOX solution was added to Fe_3O_4@GO-Cys dispersed in PBS (pH=7.4) at different drug/carrier ratios (1:1, 2:1, 3:1, 5:1, 10:1, and 20:1) separately, and the reaction was incubated at room temperature with gentle shaking. After 72 h, the mixture was centrifuged at 12,000 rpm for 15 min and washed several times with distilled water. The supernatant solution was analyzed for DOX concentration (Qe) using a UV-VIS spectrophotometer at 480 nm [43]. The drug-loading (DL) and drug-loading efficiency (LE) of the DOX were calculated as follows:

$$\mathrm{DL}\,(\%) = \frac{\mathrm{W}_{\mathrm{Loaded\ DOX}}}{\mathrm{W}_{\mathrm{DOX-loaded\ carrier}}} \times\ 100$$

$$\mathrm{LE}\,(\%) = \frac{\mathrm{W}_{\mathrm{Loaded\ DOX}}}{\mathrm{W}_{\mathrm{DOX\ added\ to\ carrier}}} \times\ 100$$

Additionally, DOX loading data at various drug/carrier ratios were fitted to different adsorption isotherms (Langmuir, Freundlich, Temkin, and Dubinin-Radushkevich). The model with the greatest goodness of fit (R^2) was chosen to investigate the mechanism of DOX loading.

DOX release

For investigation of the release manner of DOX from the prepared nanocomposite, 3 mg Fe_3O_4@GO-Cys loaded

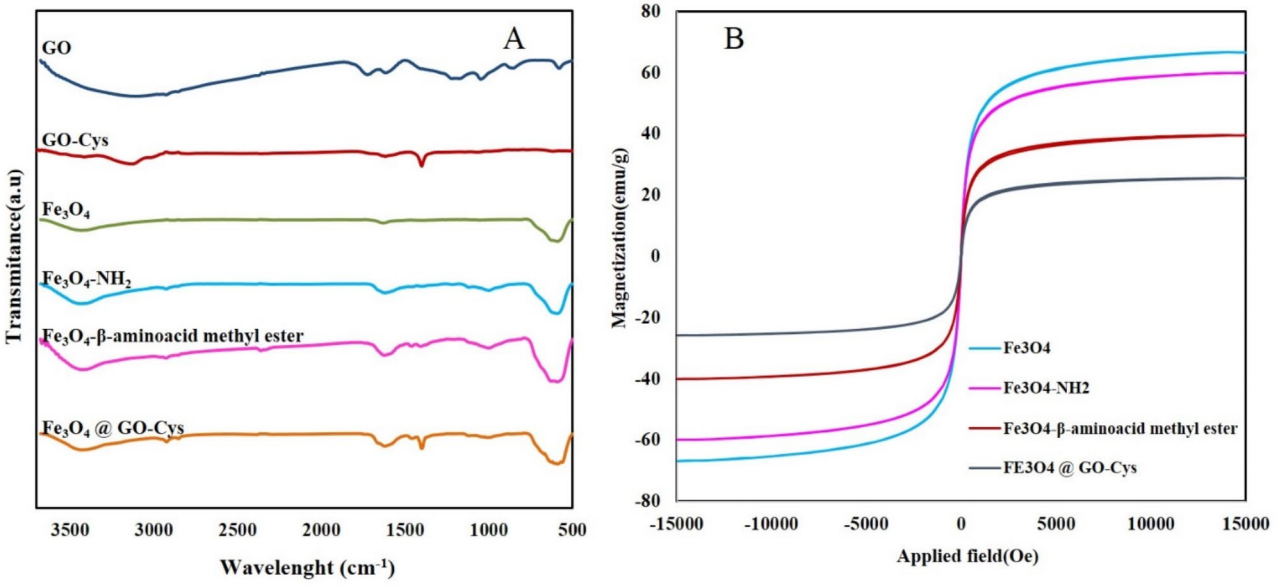

Fig. 2 (**A**) FT-IR spectra and (**B**) vibrating sample magnetometer (VSM) curves of GO, GO-Cys, Fe_3O_4, Fe_3O_4-NH_2, Fe_3O_4-β-amino acid methyl ester and Fe_3O_4@GO-Cys

with DOX was dispersed in 1 ml acetate buffer (pH 5.3) and PBS buffer (pH 7.4) in the presence or absence of 0.01 M GSH. The mixture was incubated at 37 °C with gentle shaking in a dark place. Samples were taken and centrifuged at regular intervals, and the concentration of DOX in the supernatant was measured using UV-VIS at 480 nm. The results were reported as cumulative drug release percentage versus time [44]. The release data were fitted to different kinetic models, and the best-fitted

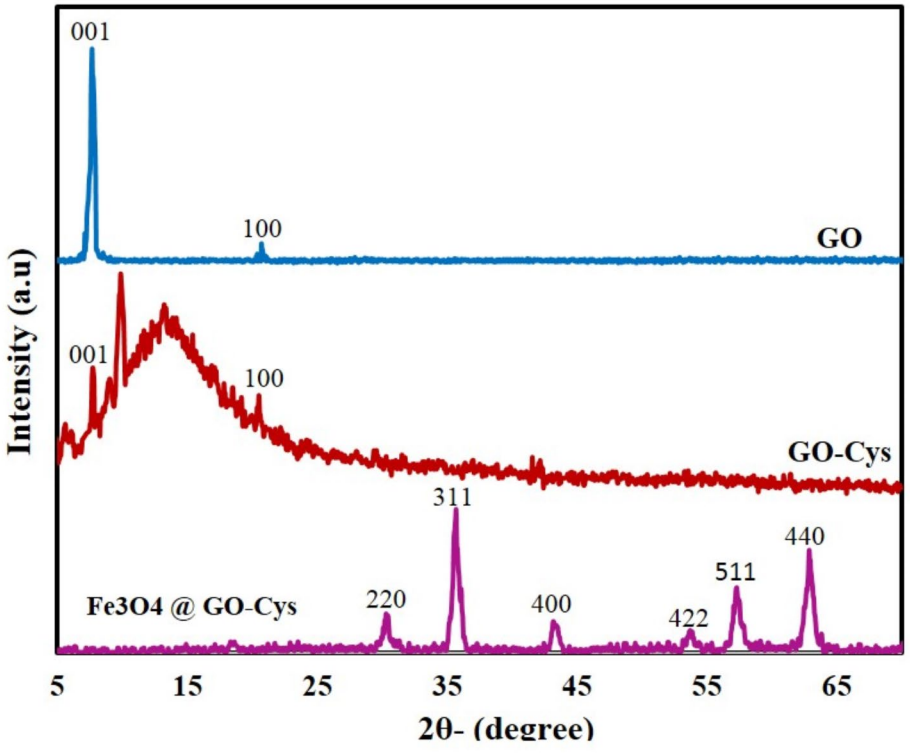

Fig. 3 XRD patterns of GO, GO-Cys, and Fe_3O_4@GO-Cys

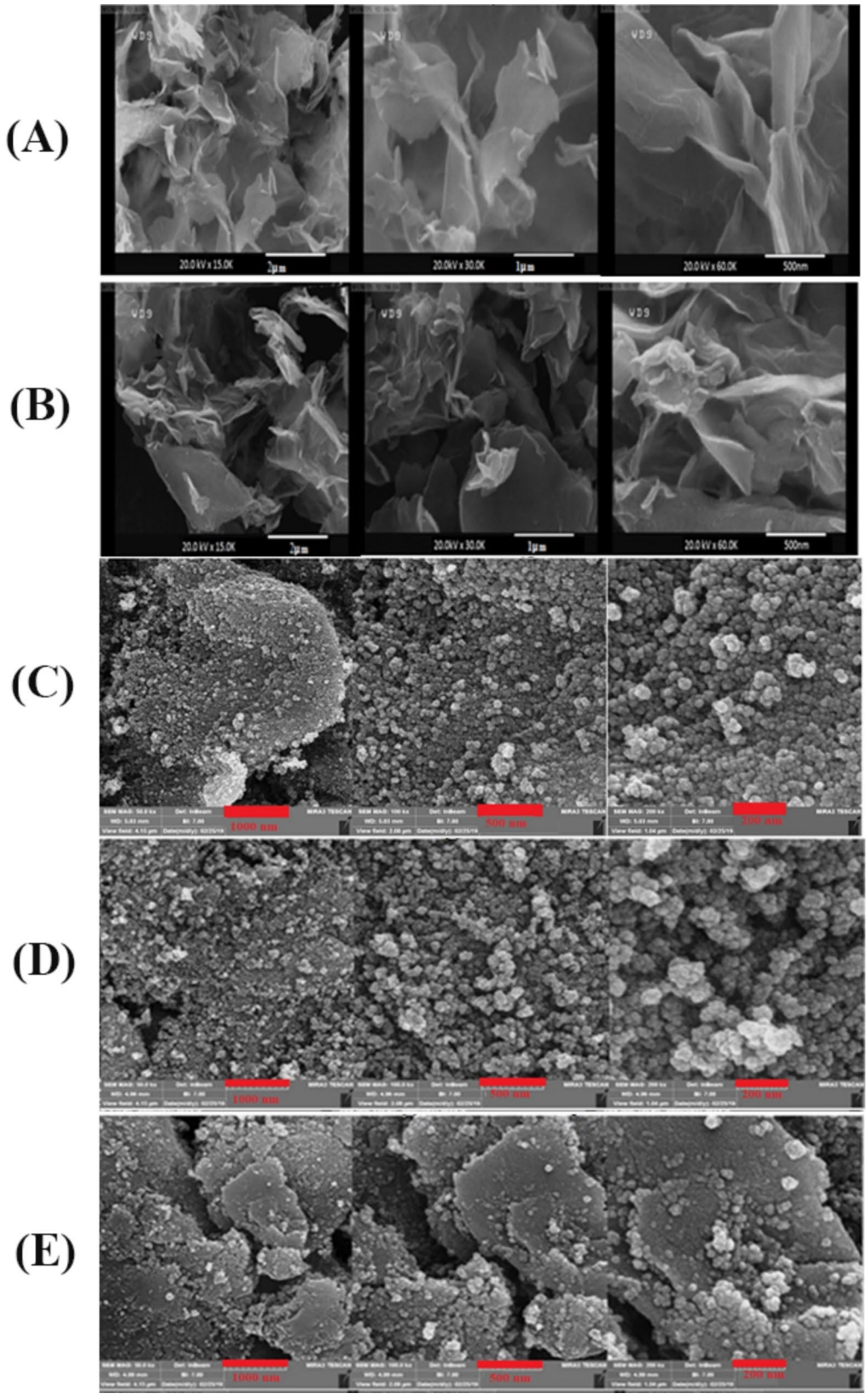

Fig. 4 FE-SEM images of (**A**) GO, (**B**) GO-Cys, (**C**) Fe_3O_4-β-amino acid methyl ester, and (**D**) Fe_3O_4@GO-Cys

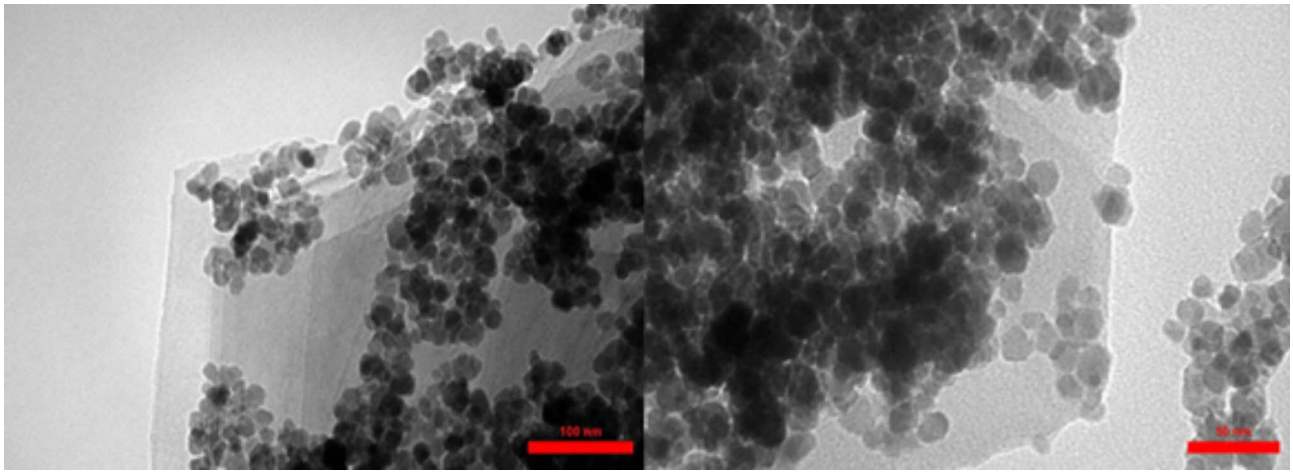

Fig. 5 TEM image of Fe_3O_4@ GO-Cys

model (the one with the highest R^2) was chosen to investigate the drug release mechanism.

Cytotoxicity assay

Briefly, HepG2 cells (2×10^4 cells/well) were seeded in 96-well microplates under standard conditions (37 °C and 5% CO_2) in RPMI 1640 medium containing L-glutamine (1% v/v) and HEPES (15 mM). The medium was supplemented with 10% heat-inactivated FBS, 100 U/mL penicillin, and 100 µg/mL streptomycin. After 24 h, the culture medium was removed, and the cells were treated with 100 µL of Fe_3O_4@ GO-Cys (unloaded or DOX-loaded), free DOX, or control PBS solution in complete culture medium, at an equivalent DOX concentration of 2, 10, 20, or 50 µl/ml [45]. After 48 h, the cell culture medium was replaced with fresh media, and MTT solution (0.5 mg/ml) was added to each well. Following a 4-hour incubation, the cell culture medium containing MTT solution was replaced with a fresh medium. The purple formazan crystals were dissolved in 100 µl of DMSO, and the absorbance was measured at 570 and 650 nm using a microplate reader.

Result and discussion

Synthesis and characterization of Fe3O4@GO-Cys

GO nanosheets were synthesized and functionalized with Cys as a GSH-sensitive linker, as reported elsewhere (Fig. 1, upper panel) [46]. In parallel, Fe_3O_4 NPs were synthesized, and a layer of silane coupling agent (APTES) was applied to create amino groups on the surface of magnetic NPs. The surface of modified Fe_3O_4 NPs was then conjugated with methyl acrylate through the Michael reaction to provide a suitable functional group for crosslinking interaction with GO-Cys (Fig. 1, lower panel). The magnetic GO nanosheets obtained, featuring generation 1 (G1) amidoamine-dendronized crosslinks, were utilized for DOX loading and release, alongside cytotoxicity experiments.

FT-IR analysis

Figure 2A depicts the FT-IR spectra of GO, GO-Cys, Fe_3O_4-CA, Fe_3O_4-NH_2, Fe_3O_4-β-amino acid methyl ester, and Fe_3O_4@GO-Cys. GO, produced through Hummer's method, exhibits hydroxyl, epoxy, and carboxylic acid groups on its surface. Specifically, GO displays a C-O stretching peak at 1033 cm^{-1}, O-H deformation at 1375 cm^{-1}, carboxyl C=O stretching at 1718 cm^{-1}, and a broad O-H stretching band at 3404 cm^{-1}. Upon modification with Cys, the appearance of an amidic C=O band at 1683 cm^{-1} and an N-H stretching band at 3445 cm^{-1} confirms the presence of Cys on the GO surface. A noticeable reduction in absorption at 1705 cm^{-1} after Cys modification suggests that the amide structure predominantly consumes the COOH groups.

In the FTIR spectrum of Fe3O4-CA, characteristic bands were observed at 582 cm^{-1}, 3404 cm^{-1}, 1711 cm^{-1}, and 1615 cm^{-1}, which correspond to Fe-O, acidic carbonyl groups, symmetric C=O stretching, and C-O of citric acid, respectively. After coating Fe_3O_4-CA with APTES, new bands due to Si-OH and Si-O-Si asymmetric stretching vibrations appeared at 2345 cm^{-1} and 1010 cm^{-1}, respectively. In addition, a characteristic band was observed at 3407 cm^{-1} corresponding to N-H stretching. The band observed at 2924 cm^{-1} in Fe_3O_4-NH_2 and β-amino acid methyl ester samples are attributed to C-C stretching vibration. In the FT-IR spectrum of Fe_3O_4@GO-Cys, the characteristic band at 580 cm^{-1} corresponds to Fe-O, the band at 1375 cm^{-1} is associated with carboxyl C=O stretching, and the O-H stretching band is observed at 3404 cm^{-1}.

Vibration sample magnetometry (VSM)

Using VSM analysis, the magnetic properties of the Fe_3O_4-CA, Fe_3O_4-NH_2, Fe_3O_4-β-amino acid methyl ester, and Fe_3O_4@GO-Cys have been investigated. From the VSM curves depicted in Fig. 2B, it can be inferred that

all the samples exhibited superparamagnetic behavior, as evidenced by the absence of hysteresis loops. The saturation magnetizations (Ms) of Fe_3O_4-CA, Fe_3O_4-NH_2, Fe_3O_4-β-amino acid methyl ester, and Fe_3O_4@GO-Cys are 66, 59, 39, and 25 emu/g, respectively. Notably, the maximum magnetic saturation value observed for Fe_3O_4-CA (66 emu/g) surpassed previously reported values in the literature [47, 48], owing to the influence of particle size and crystalline phase on magnetism saturation [49]. It is well-established that smaller particles exhibit higher magnetism saturation [50]. The coating of Fe_3O_4-CA with diamagnetic APTES compounds led to a reduction in the magnetic saturation of Fe_3O_4-NH2 NPs compared to bare Fe_3O_4-CA NPs [51]. The silica layer on magnetic NPs increased particle size and weakened dipole-dipole interactions, thereby reducing magnetism saturation [50]. In addition, modifying Fe_3O_4-NH_2 with β-amino acid methyl ester and GO-Cys decreased maximum magnetism saturation to 39 and 25 emu/g, respectively. This reduction can be attributed to the G1 amidoamine dendronized linkages on the NP surface, which increased particle size and created a dead layer between magnetic NPs, consequently decreasing magnetism saturation [51, 52].

XRD analysis

XRD analysis was conducted on the synthesized GO, GO-Cys, and Fe_3O_4@GO-Cys. The XRD patterns of GO and GO-Cys are displayed in Fig. 3. The GO XRD pattern exhibited two diffraction peaks: a wide peak at 2θ=7.8, corresponding to the (001) reflection of GO, attributed to the spacing between GO layers, and a smaller peak at 2θ=20.48, corresponding to the (002) reflection of GO [53, 54]. By modifying GO via the Cys group, the appearance of the GO diffraction peaks at 2θ=7.8 and 2θ=20.48 in the XRD pattern of GO-Cys demonstrated that the Cys modification did not have any significant effect on the crystalline structure of GO. However, in the XRD pattern of Fe_3O_4@GO-Cys, peaks related to GO disappeared, and Fe_3O_4 characteristic peaks appeared at 2θ=20.6, 30.4, 32.1, 36.6, 43.3, 53.8, 57.6, and 63.1, corresponding to the (111), (220), (222), (311), (400), (422), (511), and (440) planes of Fe_3O_4 cubic spinel surfaces [55]. Modification of GO-Cys by Fe_3O_4-β-amino acid methyl ester increased the distance between GO sheets, and the diffraction peak of GO was lost after the GO sheets were covered with Fe_3O_4 NPs, as the GO sheets could not stack on top of each other to form a crystal structure [42].

Electron microscopy

The morphology of Fe_3O_4-CA, Fe_3O_4-NH_2, Fe_3O_4-β-amino acid methyl ester, GO, GO-Cys, and Fe_3O_4@GO-Cys were examined first by the FE-SEM method, and the acquired images are presented in Fig. 4. The electron microscopy image shows the sheet-like structure of GO and GO-Cys. The FE-SEM images reveal morphological changes in the GO layer after modification with Cys. GO had a smooth surface but became wrinkled with Cys functionalization. Fe_3O_4-CA and Fe_3O_4-β-amino acid methyl ester NPs predominantly have spherical morphology with a mean particle size of 19±5 nm and 28±7 nm, respectively. In the FE-SEM and TEM images (Fig. 5) of Fe_3O_4@GO-Cys, it is evident that the Fe_3O_4-β-amino acid methyl ester NPs are firmly attached at a high density to the GO-Cys nanosheets.

Table 1 Particle size (intensity-averaged) and zeta potential of Fe_3O_4-CA, Fe_3O_4-NH_2, Fe_3O_4-β-amino acid methyl ester, GO, GO-Cys, and Fe_3O_4@GO-Cys NPs in PBS (pH=7.4)

Sample	Particle size (Mean ± SD, nm)	PDI	Zeta potential (Mean ± SD, nm)
Fe_3O_4-CA	16±3	0.12	-34.6±3.3
Fe_3O_4-NH_2	27±11	0.18	-22.7±4.5
Fe_3O_4-β-amino acid methyl ester	41±18	0.25	-34.3±1.7
GO	580±73	0.35	-55.6±4.5
GO-Cys	620±32	0.41	-46.5±5.6
Fe_3O_4@GO-Cys	759±134	0.39	-33.2±4.2

Particle size and zeta potential

The hydrodynamic diameters and zeta potentials of Fe_3O_4-CA, Fe_3O_4-NH_2, Fe_3O_4-β-amino acid methyl ester, GO, GO-Cys, and Fe_3O_4@GO-Cys dispersions in PBS (pH=7.4) were evaluated (Table 1). The average hydrodynamic diameter of GO was 580 nm, and the size of GO-Cys increased to 620 nm, with the absolute value of zeta potential decreasing from −55.6 to -46.5 mV, indicating Cys attachment to the GO surface and an increased hydrodynamic diameter. The presence of hydroxyl and carboxylate groups resulted in a negative zeta potential for GO, which decreased after Cys modification due to the charge neutralization of the Cys amino groups [22]. The mean hydrodynamic particle size of Fe_3O_4-CA was 16 nm, which increased to 27 nm after APTES coating in Fe_3O_4-NH_2 NPs. Further modification with methyl acrylate yielded Fe_3O_4-β-amino acid methyl ester with particle sizes significantly increased to 41 nm. Fe_3O_4-CA NPs exhibited a negative zeta potential of -34.6 mV in PBS due to the negative charge of the citrate groups on the particle surface, which decreased to -22.7 mV with the positively charged APTES amino groups [33]. When a β-amino acid methyl ester group was linked to Fe_3O_4-NH_2, the negative zeta potential increased to -34.3 mV possibly due to the reaction of amino groups with methyl acrylate [34]. Finally, after coupling GO-Cys to Fe_3O_4-β-amino acid methyl ester NPs, the zeta potential reached −33.2 mV [22]. This negative charge creates electrostatic repulsion

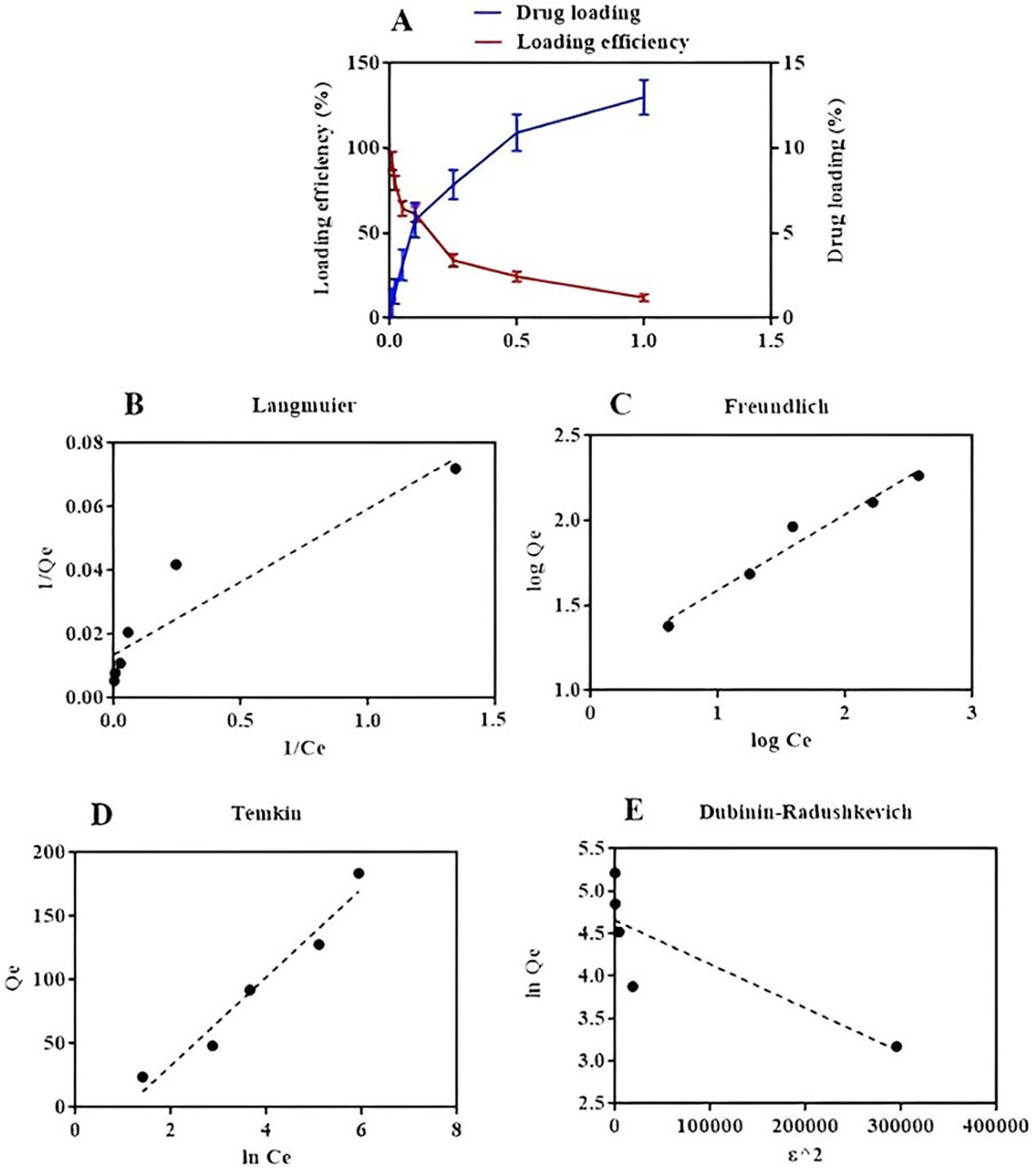

Fig. 6 (**A**) loading efficiency (LE) and drug loading (DL) of DOX into Fe_3O_4@GO-Cys NPs, (**B**) Langmuir, (**C**) Temkin, (**D**) Freundlich, and (**E**) Dubinin-Radushkevich adsorption isotherms

Table 2 DOX adsorption isotherm parameters for the Fe_3O_4 @ GO-Cys

Langmuir			Freundlich			Temkin			Dubinin-Radushkevich		
Q_m(mg/g)	K_L(L/g)	R^2	K_F(L/g)	n	R^2	K_T(L/g)	B (J/mol)	R^2	Q_s(mg/g)	K_D(mol^2/kJ^2)	R^2
21.83	0.296	0.86	0.42	0.34	0.96	0.012	38.28	0.89	158.5	0.0034	0.68

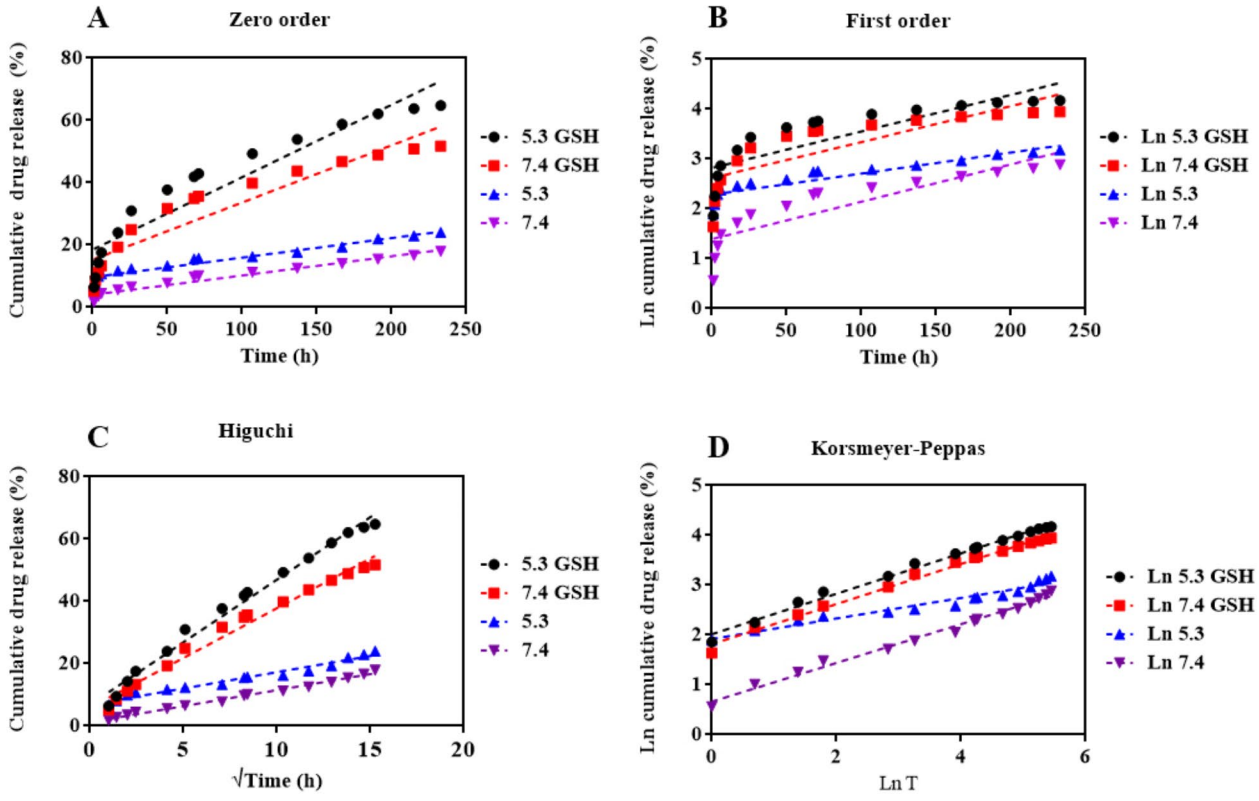

Fig. 7 DOX release from Fe_3O_4@GO-Cys NPs fitted on (**A**) zero-order, (**B**) first-order, (**C**) Higuchi, and (**D**) Korsmeyer-Peppas equations

between particles, preventing them from aggregating or flocculating. As a result, Fe_3O_4@GO-Cys tend to remain dispersed and stable in an aqueous medium because the repulsive forces between particles inhibit their tendency to come together.

Drug loading and adsorption isotherms

Figure 6. shows DOX loading (DL) and loading efficiency (LE) for Fe_3O_4@GO-Cys samples with different drug/particle ratios. As expected, increasing the drug/particle ratio increases the DL, but it results in a decrease in LE. At a drug/particle ratio of 1, the maximum DL was determined to be 13.1%. DOX can be loaded onto Fe_3O_4@GO-Cys through non-covalent π-π stacking [56]. The π electrons on the quinone group and the GO aromaticity can immobilize DOX through noncovalent adsorption. DOX molecules can also bind to GO through hydrogen bonding between the amine group of DOX and the hydroxyl and carbonyl groups of GO [57]. Additionally, the electrostatic interaction between the positive charge of the -NH2 group and the negative charge of the Fe_3O_4@GO-Cys nanocomposite allows DOX to bind to the carriers [58]. Importantly, DOX carbonyls can also form pH-sensitive Schiff-base linkages with GO-Cys amines [59]. For elucidating the DOX loading mechanism, four adsorption isotherm models (Langmuir, Freundlich, Temkin, and Dubinin-Radushkevich) were used to fit the drug loading data [60]. Table 2. shows the parameters of the equation and the coefficient of determination (R^2). As shown in Fig. 6, R^2=0.96 for Fe_3O_4@GO-Cys, indicating that the Freundlich model fits the data well. The results indicate surface heterogeneity caused by multilayer adsorption of DOX on Fe_3O_4@GO-Cys nanosheet [61].

DOX release

The cumulative release data of DOX from Fe_3O_4@GO-Cys with or without GSH (10 mmol/L) at different pH are shown in Fig. 7. DOX-loaded nanocomposite exhibited a biphasic drug release pattern, characterized by a fast release profile release followed by a slow DOX release. This initial rapid release is likely attributable to some of the DOX being physically bound to Fe_3O_4@GO-Cys NPs. Changing the pH of the release medium showed a modest alteration in the drug release profile, possibly due to the high apparent solubility of DOX in acidic media. The cumulative drug released at pH 5.3 and 7.4 in the absence of GSH after 233 h was only 24.1% and 17.9%, respectively. DOX exhibited pH-dependent release behavior, potentially because of hydrogen bonding interactions between –OH of nanocomposite with –OH and $–NH_2$ groups of DOX, or cleavage of Schiff base bonds between DOX carbonyl and Cys amine; however, the level of

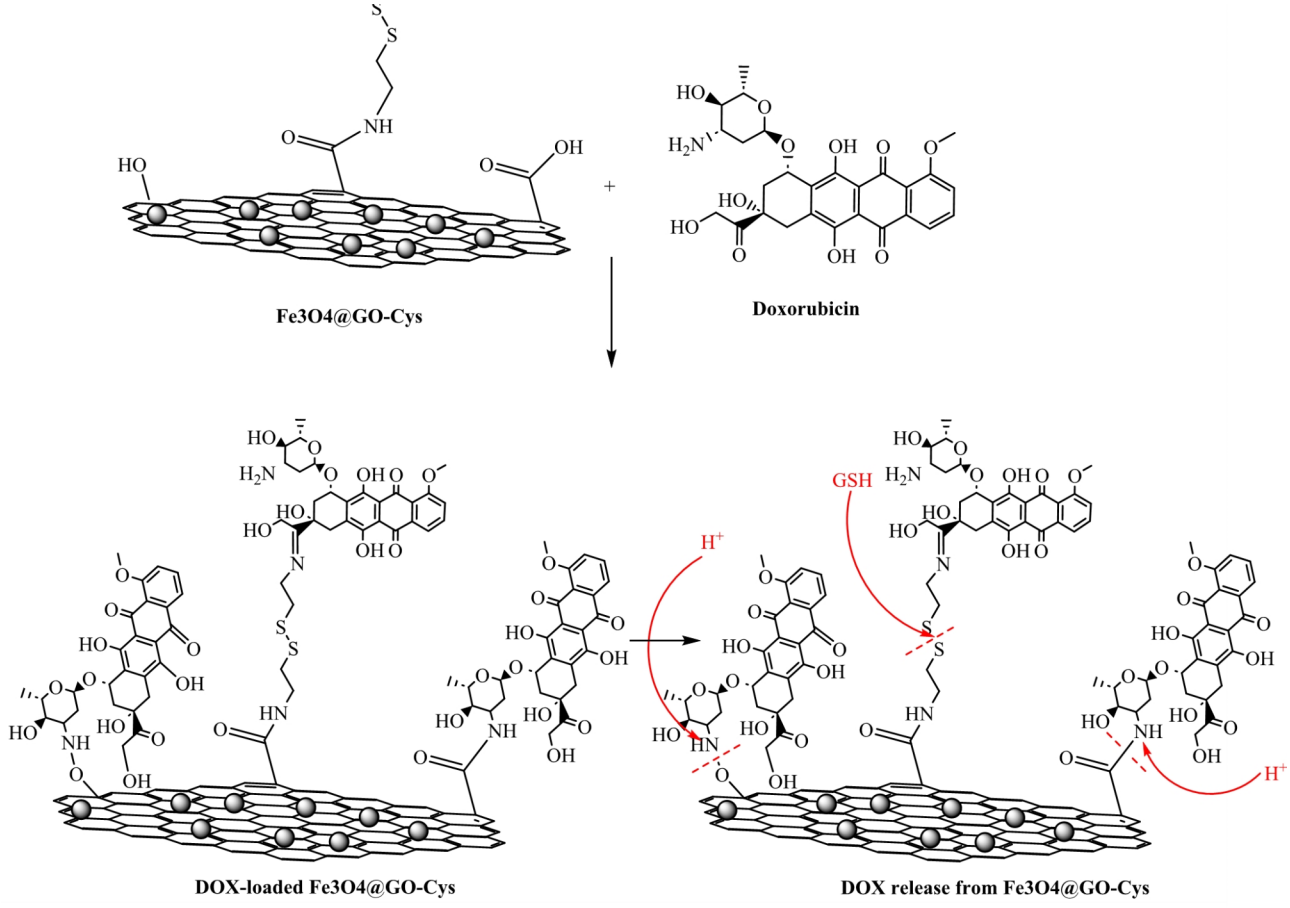

Fig. 8 Schematic presentation of DOX loading and release from Fe_3O_4@GO-Cys

Table 3 Release kinetics parameters and correlation coefficients (R^2) of DOX-loaded Fe_3O_4@GO-Cys calculated for different mathematical models

Condition	Medium pH	Zero-order		First-order		Higuchi			Korsmeyer-Peppas	
		K_0	R^2	K_1	R^2	K_h	R^2	n	K_k	R^2
Without GSH	5.3	0.2326	0.89	0.0073	0.6832	1.043	0.9873	0.405	6.6825	0.9914
	7.4	0.1836	0.87	0.0072	0.6751	1.032	0.9816	0.402	1.7545	0.9916
With GSH	5.3	0.0628	0.94	0.0042	0.8504	4.015	0.9676	0.205	7.0286	0.9519
	7.4	0.0618	0.96	0.0074	0.7759	3.193	0.9910	0.388	5.1505	0.9890

released DOX was significantly lower than our previous report [45]. This finding can be explained by the strong stacking of graphene sheets working as physical barriers to DOX diffusion and π-π interactions between DOX and nanocomposite. In the next step, to evaluate the GSH sensitivity of DOX release, the in vitro drug release was measured in media containing GSH. In the presence of GSH, the cumulative DOX significantly increased to 51.7% (2.89 folds) and 64.8% (2.69 folds) after 233 h in pH 7.4 and 5.3, respectively. These findings confirmed the -S-S bond in Cys can influence DOX release (Fig. 8), confirming DOX loading through interaction with Cys moieties. These outcomes are consistent with the previous report [45].

The first 60% of experimental DOX release data were fitted on zero-order, first-order, Higuchi, and Korsmeyer-Peppas mathematical equations to study the mechanism of DOX release from the nanocomposite. The obtained release parameters are shown in Table 3. According to the models' R^2, the Higuchi model was the best fit. As

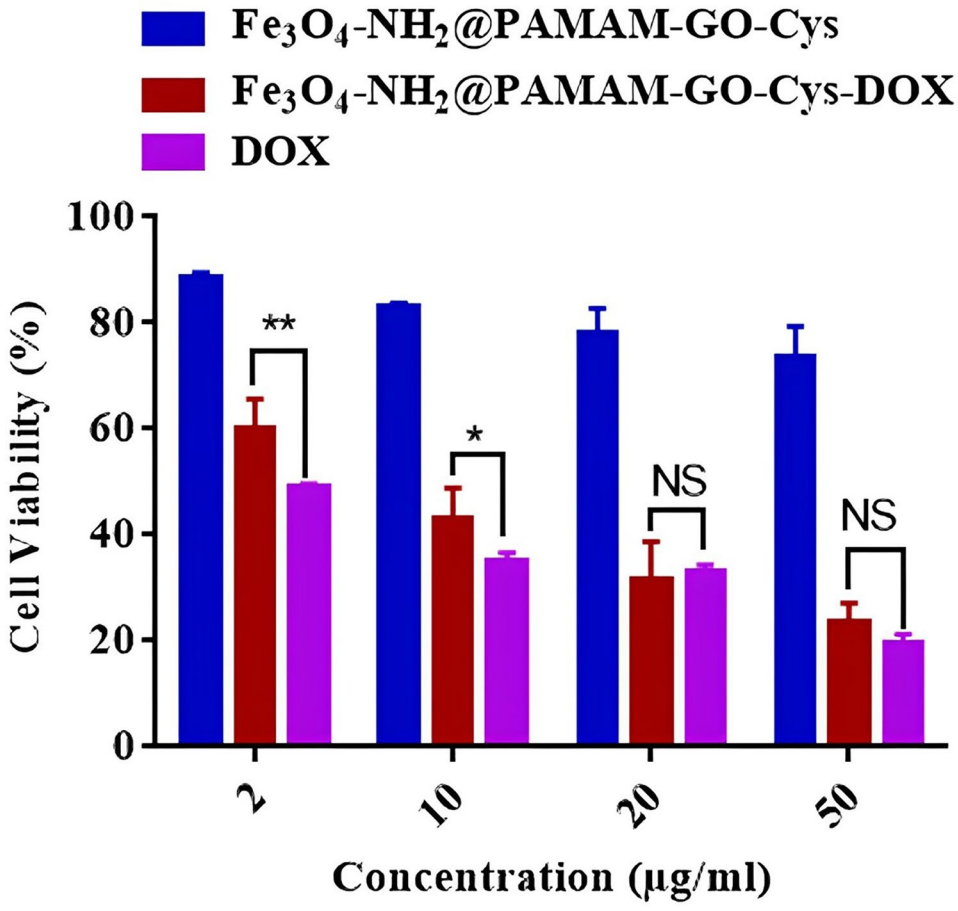

Fig. 9 MTT assay of HepG2 cell viability after 72 h exposure to different concentrations of DOX, Fe_3O_4@GO-Cys, and DOX-loaded Fe_3O_4@GO-Cys

presented in Table 3, the Korsmeyer-Peppas release exponent (n) falls between 0.3016 and 0.4329, indicating that drug release follows Fickian diffusion [62]. Moreover, in the presence of GSH, the drug release rate constant significantly increased especially at neutral pH, indicating redox-sensitive DOX release from Fe_3O_4@GO-Cys.

In-vitro cytotoxicity assay

To evaluate the effect of DOX-loaded Fe_3O_4@GO-Cys nanocomposite on HepG2 cell viability, cells were treated with free DOX, unloaded, and drug-loaded carrier for 72 h. The MTT assay showed that DOX-loaded particles effectively inhibited cancer cell growth in a concentration-dependent manner (Fig. 9), which was comparable to free DOX. The unloaded Fe_3O_4@GO-Cys nanocomposites exhibited minor cytotoxicity even at a final concentration of 50 µg/mL, ensuring that the synthesized nanocarriers showed minor cytotoxicity in the biological medium. IC_{50} values were calculated to be 3.79 ± 0.29 and 1.88 ± 0.24 µM for free DOX and DOX-loaded Fe_3O_4@GO-Cys nanocomposites, respectively, which are similar to the previously reported IC_{50} = 3.4 µM for DOX-loaded GO [63]. This result is consistent with other reports, which demonstrate an IC_{50} value of 3.8 ± 0.37 µM for free DOX on the HepG2 cell line [64]. However, the effectiveness of DOX-loaded nanocomposite was higher than free DOX which can be due to the nanoscale effect resulting in the cellular drug internalization with different mechanisms from free drug [65].

Conclusion

A novel class of superparamagnetic iron oxide-decorated GO-Cys nanocomposites, characterized by high drug loading and redox reactivity, has been developed, demonstrating an outstanding in vitro antitumor effect. Incorporating Cys disulfide bonds imparted redox sensitivity to the prepared nanocomposite, promoting drug release by adding 10 mmol/L GSH. Additionally, cell viability experiments indicated that this magnetic nanocomposite (Fe_3O_4@GO-Cys) exhibits good biocompatibility while demonstrating acceptable anticancer activity against HepG2 cancer cells. Therefore, this carrier holds promise for further in vivo studies.

Acknowledgements
We also gratefully acknowledge the use of the Center for Nanotechnology in Drug Delivery facilities at SUMS.

Author contributions
Amir Reza Sarikhani: Methodology, Validation, Formal analysis, Investigation Writing - original draft, Mehdi Abedi: Methodology, Investigation, Data curation, Formal analysis, Visualization, Writing - original draft. Sedigheh Borandeh: Conceptualization, Methodology, Formal analysis, Investigation, Writing – review & editing. Samira Sadat Abolmaali: Conceptualization, Supervision, Writing – review & editing. Ali Mohammad Tamaddon: Conceptualization, Supervision, Methodology, Formal analysis, Investigation, Writing – review & editing, Funding acquisition.

Funding
This work was supported by Grant No 13584, Shiraz University of Medical Sciences (SUMS).

Data availability
The datasets used and/or analyzed during the current study are available from the corresponding author on reasonable request. The datasets used and/or analyzed during the current study are available from the corresponding author on reasonable request.

Declarations

Ethics approval and consent to participate
Not applicable.

Consent for publication
Not applicable.

Competing interests
The authors declare no competing interests.

Received: 3 April 2024 / Accepted: 18 September 2024
Published online: 28 September 2024

References

1. Siegel RL, Giaquinto AN, Jemal A. Cancer statistics, 2024. CA Cancer J Clin. 2024;74(1):12–49.
2. Arabestanino AR, Naghibi Irvani SS, Ai A, Dinarvand B. Structural carcinoma overall process: a systematic review. Cell Mol Biomedical Rep. 2024;4(2):88–99.
3. Ali Salman R. Prevalence of women breast cancer. Cell Mol Biomedical Rep. 2023;3(4):185–96.
4. Li X, Li D. Natural compounds targeting cellular redox homeostasis in malignancies. Cell Mol Biol (Noisy-le-grand). 2023;69(14):255–65.
5. Eralp TN, Sevinc A, Mansuroglu B. Combination therapy application of Abemaciclib with Doxorubicin in triple negative breast cancer cell line MDA-MB-231. Cell Mol Biol (Noisy-le-grand). 2024;70(2):169–77.
6. Sun G, Gong S, Lan S, He Y, Sun Y, Zhang Z. TMCO1 regulates cell proliferation, metastasis and EMT signaling through CALR, promoting ovarian cancer progression and cisplatin resistance. Cell Mol Biol (Noisy-le-grand). 2024;70(1):99–109.
7. Reddy KTK, Reddy AS. Recent breakthroughs in drug delivery systems for targeted cancer therapy: an overview. Cell Mol Biomedical Rep 2024:13–27.
8. Alavi M, Rai M, Martinez F, Kahrizi D, Khan H, Rose Alencar de Menezes I, Douglas Melo Coutinho H, Costa J. The efficiency of metal, metal oxide, and metalloid nanoparticles against cancer cells and bacterial pathogens: different mechanisms of action. Cell Mol Biomedical Rep. 2022;2(1):10–21.
9. Hami Z. A brief review on advantages of Nano-based Drug Delivery systems. Annals Military Health Sci Res. 2021;19(1):e112274.
10. Hoseini-Ghahfarokhi M, Mirkiani S, Mozaffari N, Abdolahi Sadatlu MA, Ghasemi A, Abbaspour S, Akbarian M, Farjadian F, Karimi M. Applications of Graphene and Graphene Oxide in Smart Drug/Gene Delivery: is the World still flat? Int J Nanomed. 2020;15:9469–96.
11. Abdollahzade A, Rahimi H, Yaghoobi E, Ramezani M, Alibolandi M, Abnous K, Taghdisi SM. Targeted delivery of doxorubicin and therapeutic FOXM1 aptamer to tumor cells using gold nanoparticles modified with AS1411 and ATP aptamers. Iran J Basic Med Sci. 2023;26(10):1177–87.
12. Abdelfattah A, Aboutaleb AE, Abdel-Aal ABM, Abdellatif AAH, Tawfeek HM, Abdel-Rahman SI. Design and optimization of PEGylated silver nanoparticles for efficient delivery of doxorubicin to cancer cells. J Drug Deliv Sci Technol. 2022;71:103347.
13. Khabibullin VR, Chetyrkina MR, Obydennyy SI, Maksimov SV, Stepanov GV, Shtykov SN. Study on Doxorubicin Loading on differently Functionalized Iron Oxide nanoparticles: implications for controlled drug-delivery application. Int J Mol Sci. 2023;24(5):4480.
14. Hazeri Y, Samie A, Ramezani M, Alibolandi M, Yaghoobi E, Dehghani S, Zolfaghari R, Khatami F, Zavvar T, Nameghi MA, et al. Dual-targeted delivery of doxorubicin by mesoporous silica nanoparticle coated with AS1411 aptamer and RGDK-R peptide to breast cancer in vitro and in vivo. J Drug Deliv Sci Technol. 2022;71:103285.
15. Cavalcante CH, Fernandes RS, de Oliveira Silva J, Ramos Oda CM, Leite EA, Cassali GD, Charlie-Silva I, Ventura Fernandes BH, Miranda Ferreira LA, de Barros ALB. Doxorubicin-loaded pH-sensitive micelles: a promising alternative to enhance antitumor activity and reduce toxicity. Biomed Pharmacother. 2021;134:111076.
16. Abolmaali S, Tamaddon A, Salmanpour M, Mohammadi S, Dinarvand R. Block Ionomer micellar nanoparticles from double hydrophilic copolymers, classifications and promises for delivery of cancer chemotherapeutics. Eur J Pharm Sci. 2017;104:393–405.
17. Zaer M, Moeinzadeh A, Abolhassani H, Rostami N, Tavakkoli Yaraki M, Seyedi SA, Nabipoorashrafi SA, Bashiri Z, Moeinabadi-Bidgoli K, Moradbeygi F, et al. Doxorubicin-loaded niosomes functionalized with gelatine and alginate as pH-responsive drug delivery system: a 3D printing approach. Int J Biol Macromol. 2023;253:126808.
18. Michlewska S, Garaiova Z, Šubjakova V, Hołota M, Kubczak M, Grodzicka M, Okła E, Naziris N, Balcerzak Ł, Ortega P, et al. Lipid-coated ruthenium dendrimer conjugated with doxorubicin in anti-cancer drug delivery: introducing protocols. Colloids Surf B. 2023;227:113371.
19. Dehghankhold M, Ahmadi F, Nezafat N, Abedi M, Iranpour P, Dehghanian A, Koohi-Hosseinabadi O, Akbarizadeh AR, Sobhani Z. A versatile theranostic magnetic polydopamine iron oxide NIR laser-responsive nanosystem containing doxorubicin for chemo-photothermal therapy of melanoma. Biomaterials Adv. 2024;159:213797.
20. Chadar R, Afzal O, Alqahtani SM, Kesharwani P. Carbon nanotubes as an emerging nanocarrier for the delivery of doxorubicin for improved chemotherapy. Colloids Surf B. 2021;208:112044.
21. Mahani M, Pourrahmani-Sarbanani M, Yoosefian M, Divsar F, Mousavi SM, Nomani A. Doxorubicin delivery to breast cancer cells with transferrin-targeted carbon quantum dots: an in vitro and in silico study. J Drug Deliv Sci Technol. 2021;62:102342.
22. Rai S, Guin M, De A, Singh NB. Functionalized nanomaterials: basics, Properties and Applications. Functionalized nanomaterials for Corrosion Mitigation: synthesis, characterization, and applications. Volume 1418. edn.: American Chemical Society; 2022. pp. 27–66.
23. Hatamie S, Balasi ZM, Ahadian MM, Mortezazadeh T, Shams F, Hosseinzadeh S. Hyperthermia of breast cancer tumor using graphene oxide-cobalt ferrite magnetic nanoparticles in mice. J Drug Deliv Sci Technol. 2021;65:102680.
24. Zhang H, Fan T, Chen W, Li Y, Wang B. Recent advances of two-dimensional materials in smart drug delivery nano-systems. Bioact Mater. 2020;5(4):1071–86.
25. Liu Z, Rios-Carvajal T, Andersson P, Ceccato M, Stipp M, Hassenkam SLS. Ion effects on molecular interaction between graphene oxide and organic molecules. Environ Science: Nano. 2019;6(7):2281–91.
26. Adel-Mehraban F, Raeissi K, Karimzadeh F, Pedersen SU, Salehzadeh H, Daasbjerg K. A novel approach toward attachment of graphene oxide on copper using electrochemical grafting of an organic interlayer with enhanced corrosion performance. Prog Org Coat. 2021;154:106185.
27. Ranishenka B, Ulashchik E, Tatulchenkov M, Sharko O, Panarin A, Dremova N, Shmanai V. Graphene oxide functionalization via epoxide ring opening in bioconjugation compatible conditions. FlatChem. 2021;27:100235.
28. Patel KP, Gayakwad EM, Shankarling GS. Graphene Oxide as a metal-free Carbocatalyst for Direct Amide synthesis from Carboxylic Acid and Amine under Solvent-free reaction Condition. ChemistrySelect. 2020;5(27):8295–300.
29. Kukielski M, Kasprzak A, Zurowski R, Tanska J, Wiecinska P, Wieclaw-Midor A, Zygmuntowicz J, Grigoroscuta MA, Wiecinski P. Functionalization of graphene oxide surface by conjugation with glucosamine and analysis of interactions

occurring in nanoceramic-graphene heterostructures. Powder Technol. 2024;431:119089.
30. Yu W, Sisi L, Haiyan Y, Jie L. Progress in the functional modification of graphene/graphene oxide: a review. RSC Adv. 2020;10(26):15328–45.
31. Huang P, Jia H, Wang T, Xu Y, Zhang L, Wei X, Jia H, Wen S, Lv K, Liu D. Effects of Modification degrees on the Colloidal Stability of Amphiphilic Janus Graphene Oxide in Aqueous solution with and without Electrolytes. Langmuir. 2021;37(33):10061–70.
32. Karimi S, Namazi H. Fe3O4@PEG-coated dendrimer modified graphene oxide nanocomposite as a pH-sensitive drug carrier for targeted delivery of doxorubicin. J Alloys Compd. 2021;879:160426.
33. Jedrzejczak-Silicka M, Szymańska K, Mijowska E, Rakoczy R. The influence of Graphene Oxide-Fe(3)O(4) differently conjugated with 10-Hydroxycamptothecin and a rotating magnetic field on Adenocarcinoma cells. Int J Mol Sci 2024, 25(2).
34. Swain AK, Pradhan L, Bahadur D. Polymer stabilized Fe3O4-Graphene as an amphiphilic drug carrier for Thermo-Chemotherapy of Cancer. ACS Appl Mater Interfaces. 2015;7(15):8013–22.
35. Ma X, Tao H, Yang K, Feng L, Cheng L, Shi X, Li Y, Guo L, Liu Z. A functionalized graphene oxide-iron oxide nanocomposite for magnetically targeted drug delivery, photothermal therapy, and magnetic resonance imaging. Nano Res. 2012;5(3):199–212.
36. Hummers WS, Offeman RE. Preparation of Graphitic Oxide. J Am Chem Soc. 2002;80(6):1339–1339.
37. Yang X, Zhao N, Xu FJ. Biocleavable graphene oxide based-nanohybrids synthesized via ATRP for gene/drug delivery. Nanoscale. 2014;6(11):6141–50.
38. Abedi M, Abolmaali SS, Abedanzadeh M, Farjadian F, Mohammadi Samani S, Tamaddon AM. Core-Shell Imidazoline-Functionalized Mesoporous silica Superparamagnetic Hybrid nanoparticles as a potential Theranostic Agent for Controlled Delivery of platinum(II) compound. Int J Nanomed. 2020;15:2617–31.
39. Kheirkhah S, Abedi M, Zare F, Salmanpour M, Abolmaali SS, Tamaddon AM. Surface engineered palmitoyl-mesoporous silica nanoparticles with supported lipid bilayer coatings for high-capacity loading and prolonged release of dexamethasone: a factorial design approach. J Drug Deliv Sci Technol. 2022;78:103943.
40. Villa S, Riani P, Locardi F, Canepa F. Functionalization of Fe3O4 NPs by silanization: Use of Amine (APTES) and thiol (MPTMS) Silanes and their physical characterization. Materials. 2016;9(10):826.
41. Abu-Reziq R, Alper H, Wang D, Post ML. Metal supported on dendronized magnetic nanoparticles: highly selective hydroformylation catalysts. J Am Chem Soc. 2006;128(15):5279–82.
42. Aliyari E, Alvand M, Shemirani F. Modified surface-active ionic liquid-coated magnetic graphene oxide as a new magnetic solid phase extraction sorbent for preconcentration of trace nickel. RSC Adv. 2016;6(69):64193–202.
43. Borandeh S, Abdolmaleki A, Abolmaali SS, Tamaddon AM. Synthesis, structural and in-vitro characterization of beta-cyclodextrin grafted L-phenylalanine functionalized graphene oxide nanocomposite: a versatile nanocarrier for pH-sensitive doxorubicin delivery. Carbohydr Polym. 2018;201:151–61.
44. Shafiee M, Abolmaali SS, Tamaddon AM, Abedanzadeh M, Abedi M. One-pot synthesis of poly(alkyl methacrylate)-functionalized mesoporous silica hybrid nanocomposites for microencapsulation of poorly soluble phytochemicals. Colloid Interface Sci Commun. 2020;37:100298.
45. Borandeh S, Hosseinbeigi H, Abolmaali SS, Monajati M, Tamaddon AM. Steric stabilization of β-cyclodextrin functionalized graphene oxide by host-guest chemistry: a versatile supramolecule for dual-stimuli responsive cellular delivery of doxorubicin. J Drug Deliv Sci Technol. 2021;63:102536.
46. Wei H, Wang X, Liu Q, Mei Y, Lu Y, Guo Z. Disulfide bond cleavage induced by a platinum(II) methionine complex. Inorg Chem. 2005;44(17):6077–81.
47. Dheyab MA, Aziz AA, Jameel MS, Noqta OA, Khaniabadi PM, Mehrdel B. Simple rapid stabilization method through citric acid modification for magnetite nanoparticles. Sci Rep. 2020;10(1):10793.
48. Nigam S, Barick KC, Bahadur D. Development of citrate-stabilized Fe3O4 nanoparticles: conjugation and release of doxorubicin for therapeutic applications. J Magn Magn Mater. 2011;323(2):237–43.
49. Kalantari K, Ahmad MB, Shameli K, Hussein MZB, Khandanlou R, Khanehzaei H. Size-controlled synthesis of Fe3O4Magnetic nanoparticles in the layers of Montmorillonite. J Nanomaterials. 2014;2014:1–9.
50. Li L, Mak KY, Leung CW, Chan KY, Chan WK, Zhong W, Pong PWT. Effect of synthesis conditions on the properties of citric-acid coated iron oxide nanoparticles. Microelectron Eng. 2013;110:329–34.
51. Thangaraj B, Jia Z, Dai L, Liu D, Du W. Effect of silica coating on Fe3O4 magnetic nanoparticles for lipase immobilization and their application for biodiesel production. Arab J Chem. 2019;12(8):4694–706.
52. Rebekah A, Sivaselvam S, Viswanathan C, Prabhu D, Gautam R, Ponpandian N. Magnetic nanoparticle-decorated graphene oxide-chitosan composite as an efficient nanocarrier for protein delivery. Colloids Surf a. 2021;610:125913.
53. Siburian R, Sihotang H, Lumban Raja S, Supeno M, Simanjuntak C. New Route to synthesize of Graphene Nano sheets. Orient J Chem. 2018;34(1):182–7.
54. Yan H, Bai J, Liao M, He Y, Liu Q, Liu J, Zhang H, Li Z, Wang J. One-step synthesis of Co3O4/Graphene aerogels and their all-solid-state asymmetric supercapacitor. Eur J Inorg Chem. 2017;2017(8):1143–52.
55. Abedi M, Abolmaali SS, Abedanzadeh M, Borandeh S, Samani SM, Tamaddon AM. Citric acid functionalized silane coupling versus post-grafting strategy for dual pH and saline responsive delivery of cisplatin by Fe(3)O(4)/carboxyl functionalized mesoporous SiO(2) hybrid nanoparticles: A-synthesis, physicochemical and biological characterization. Mater Sci Eng C Mater Biol Appl. 2019;104:109922.
56. Zainal-Abidin MH, Hayyan M, Ngoh GC, Wong WF. Doxorubicin Loading on Functional Graphene as a Promising Nanocarrier using Ternary Deep Eutectic Solvent systems. ACS Omega. 2020;5(3):1656–68.
57. Hutchins KM. Functional materials based on molecules with hydrogen-bonding ability: applications to drug co-crystals and polymer complexes. R Soc Open Sci. 2018;5(6):180564.
58. Mei H, Cai S, Huang D, Gao H, Cao J, He B. Carrier-free nanodrugs with efficient drug delivery and release for cancer therapy: from intrinsic physicochemical properties to external modification. Bioact Mater. 2022;8:220–40.
59. Mahmoud ME, Attia AA, Helmy MW, Hemdan IH, Abouelanwar ME. Doxorubicin drug release behavior from amino-silanated graphene oxide nanocarrier. Diam Relat Mater. 2023;131:109569.
60. Behzadnia M, Salmanpour M, Heidari M, Monajati M, Farjadian F, Abedi M, Tamaddon AM. Sorafenib tosylate incorporation into mesoporous starch xerogel for in-situ micronization and oral bioavailability enhancement. Drug Dev Ind Pharm. 2022;48(8):343–54.
61. Anah L, Astrini N. Isotherm adsorption studies of Ni(II) ion removal from aqueous solutions by modified carboxymethyl cellulose hydrogel. IOP Conference Series: Earth and Environmental Science 2018;160:012017.
62. Abedi M, Abolmaali SS, Heidari R, Mohammadi Samani S, Tamaddon AM. Hierarchical mesoporous zinc-imidazole dicarboxylic acid MOFs: surfactant-directed synthesis, pH-responsive degradation, and drug delivery. Int J Pharm. 2021;602:120685.
63. Georgieva M, Vasileva B, Speranza G, Wang D, Stoyanov K, Draganova-Filipova M, Zagorchev P, Sarafian V, Miloshev G, Krasteva N. Amination of Graphene Oxide leads to increased cytotoxicity in Hepatocellular Carcinoma cells. Int J Mol Sci 2020, 21(7).
64. Omar WM, Ahmed AE, Raslan M, El-Nesr K, Ali MM, De Abdelmaksoud M, El Dahshan D. Effect of Lutein-Rich Extract on Human Cancer cells. Middle East J Cancer. 2021;12(1):147–50.
65. Chen J, Yang X, Huang L, Lai H, Gan C, Luo X. Development of dual-drug-loaded stealth nanocarriers for targeted and synergistic anti-lung cancer efficacy. Drug Delivery. 2018;25(1):1932–42.

Publisher's note